Shafi, Abde Mayeen; Das, Susobhan; Khayrudinov, Vladislav; Uddin, Md Gius; Ding, Er-Xiong; Ahmed, Faisal; Sun, Zhipei; Lipsanen, Harri

Direct Epitaxial Growth of InP Nanowires on MoS2 with Strong Nonlinear Optical Response

Published in:
Chemistry of Materials

DOI:
10.1021/acs.chemmater.2c01602

Published: 25/10/2022

Document Version
Publisher's PDF, also known as Version of record

CHEMISTRY OF MATERIALS

pubs.acs.org/cm

Article

Direct Epitaxial Growth of InP Nanowires on MoS_2 with Strong Nonlinear Optical Response

Abde Mayeen Shafi,* Susobhan Das, Vladislav Khayrudinov, Er-Xiong Ding, Md Gius Uddin, Faisal Ahmed, Zhipei Sun, and Harri Lipsanen*

Cite This: *Chem. Mater.* 2022, 34, 9055−9061

Read Online

ACCESS | Metrics & More | Article Recommendations | Supporting Information

ABSTRACT: Mixed-dimensional van der Waals heterostructures are promising for research and technological advances in photonics and optoelectronics. Here we report vapor−liquid−solid (VLS) method-based van der Waals epitaxy of one-dimensional InP nanowires (NWs) directly on two-dimensional MoS_2. With optimized growth parameters (V/III ratio, flow rates of precursors, and growth temperature), we successfully grow high-quality InP NWs on MoS_2. The density and vertical yield of NWs on MoS_2 are significantly high. Due to the unique properties of both materials, we observe strong linear and nonlinear optical responses from the NW/MoS_2 heterostructures. Intriguingly, in addition to strong second and third harmonic responses, the mixed-dimensional heterostructures show odd-order high harmonic generation up to seventh order. Our findings can open new possibilities for advancing attosecond physics on a new platform of mixed-dimensional heterostructures.

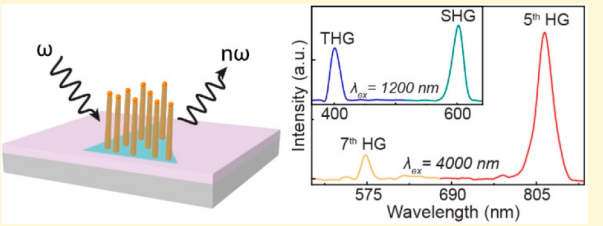

INTRODUCTION

The discovery of graphene in 2004 created a landscape of atomically thin two-dimensional (2D) materials for exotic fundamental studies and numerous applications owing to their unique optical, electronic, and physical properties.[1] Among the large number of materials in the 2D family, the layered transition-metal dichalcogenides (TMDCs) are the most extensively studied after graphene. The atomic thickness and tunable band gap spanning from near-infrared to visible regions make TMDCs a potential building block for a plethora of nanoelectronic and photonic devices.[2−7] Additionally, these materials exhibit outstanding properties such as strong intralayer covalent bonds between atoms and weak van der Waals (vdW) forces between layers, indirect-to-direct band gap transition from the bulk to the monolayer, and strong photoluminescence (PL) in monolayers because of quantum confinement.[8] 2D materials possess inherently dangling-bond-free surfaces and can form vdW heterostructures with distinct 2D and non-2D (e.g., 0-, 1- and 3-dimensional) materials circumventing lattice matching requirements. Such on-demand heterostructures provide unprecedented opportunities for next-generation optoelectronics.[9−12]

III−V semiconductor nanowires (NWs) possess excellent light trapping properties, low density of crystal defects, long-term stability, high carrier mobility, and relaxed lattice matching conditions due to their small footprint.[13−16] These unique properties make NWs promising and suitable to be grown on different foreign substrates, including atomically thin 2D materials, e.g., graphene and MoS_2.[17−23] Intriguingly, when 1D NWs are combined with 2D TMDCs having mechanical flexibility and tunable optical properties, the mixed-dimensional heterostructure can produce high-performance photonic and optoelectronic devices with complementary characteristics.[24,25] However, controlling the growth of NWs on 2D materials for achieving high vertical yield is still very challenging due to the absence of nucleation sites. Additionally, the stability of 2D materials after NW growth (especially in TMDCs) is another important issue to consider for utilizing the benefit of the mixed-dimensional heterostructures.

Being a direct bandgap material with very low surface recombination velocity and excellent optical quality,[26] InP nanowires provide a superior platform for many applications such as solar cells,[27] light-emitting diodes,[28] photodetectors,[29] and lasers.[30] In the class of 2D materials, MoS_2 is one of the well-studied TMDCs because of having a direct bandgap in monolayers, large excitonic binding energy, strong luminescence emission, and high carrier mobility.[31,32] Additionally, the nonlinear optical properties of both InP and MoS_2 are quite fascinating for many photonic applications.[33−35] Therefore, mixed-dimensional heterostructures based on InP NWs and MoS_2 show unprecedented prospects in advanced photonic research.

Received: May 28, 2022
Revised: September 30, 2022
Published: October 13, 2022

In this work, we demonstrate mixed-dimensional heterostructures consisting of vdW-epitaxially grown InP NWs on chemical vapor deposition (CVD)-grown monolayer MoS_2. The Au nanoparticle-assisted low-temperature growth produces high-quality vertical NWs on MoS_2 while ensuring the thermal and chemical stability of MoS_2. The heterostructures show excellent linear optical responses (i.e., Raman and PL). We also observe strong nonlinear optical phenomena such as second and third harmonic generations (SHG, THG) from the heterostructures. Interestingly, the heterostructures generate odd-order high harmonic (HHG) up to the seventh order. These results manifest the potential of epitaxially grown mixed-dimensional heterostructure for nanophotonics.

EXPERIMENTAL DETAILS

Monolayer (ML) and few-layer (FL) MoS_2 are grown on Si substrate covered with 285 nm of SiO_2.[36] The precursors used for growing MoS_2 flakes are Na_2MoO_4 (99.9%, Sigma-Aldrich) and sulfur powder (99.5%, Alfa Aesar). First, we clean the SiO_2/Si substrates with acetone and 2-propanol, followed by O_2 plasma treatment for surface activation. The substrates are immediately spin-coated with Na_2MoO_4 solution (density 10 mg mL^{-1}) at 4000 rpm for 1 min. The growth is carried out in a dual-zone CVD furnace with a 50 mm diameter and 200 cm long quartz tube. A schematic of the system is presented in Figure S1. We load an aluminum boat containing ∼100 mg sulfur powder in the upstream (zone 1) of 70 sccm Ar flow. The substrate is placed in the growth zone (zone 2). Zone 1 and zone 2 are heated to 180 °C and 775 °C, respectively, with a 10 °C min^{-1} ramping rate in zone 2. The temperatures in both zones are maintained for 10 min when the temperatures reach the maximum. Afterward, the furnace is cooled naturally to room temperature. The size of the as-grown triangular MoS_2 flakes varies in the range of 10−100 μm.

We grow InP NWs on MoS_2 in a horizontal flow atmospheric pressure metalorganic vapor-phase epitaxy (MOVPE) system.[19,37] As catalysts for the vapor−liquid−solid (VLS) growth, 40 nm diameter gold (Au) nanoparticles from a colloidal solution (BBI International, UK) are used. Before the spin coating of Au nanoparticles, poly-L-lysine (PLL) solution is dropped onto the MoS_2 containing a substrate for better adhesion of the particles to the substrate, which is then kept in the air for 30 s. Trimethylindium (TMIn) and tertiarybutylphosphine (TBP) are used as the precursors for growing InP NWs. To grow NWs, the precursors are inserted in the reactor simultaneously for 300 s while the reactor temperature is kept at 430 °C, and the nominal V/III ratio is ∼200 by adjusting the flow rates of TMIn and TBP to 80 and 100 sccm, respectively. We use hydrogen (H_2) as a carrier gas, and the total reactor gas flow rate in the 1-in. horizontal reactor is ∼5 L/min (slm). The temperatures reported in this work are thermocouple readings of the lamp-heated graphite susceptor, which are slightly higher than the actual substrate surface temperature.

RESULTS AND DISCUSSION

Figure 1a shows a schematic of epitaxially grown NW/MoS_2 mixed-dimensional heterostructure. The scanning electron microscopy (SEM) image of an as-grown MoS_2 single crystal is presented in Figure 1b. The growth temperature and the amount of precursors during the CVD growth process are favorable for growing ∼10−100 μm size triangular shaped of mono- and few-layer MoS_2 single crystals. Figure 1c presents the 45° tilted-view SEM image of as-grown InP NWs on the MoS_2 flake. The average height of the grown NWs is measured as ∼8 μm, and the yield of vertically aligned NWs is significantly high (∼1/μm^2). The density of the NWs is nearly homogeneous all over the monolayer MoS_2. The TEM image of the NW is shown in Figure 2a. The Au nanoparticle sitting on the NW tip is visible in the image. The high-resolution

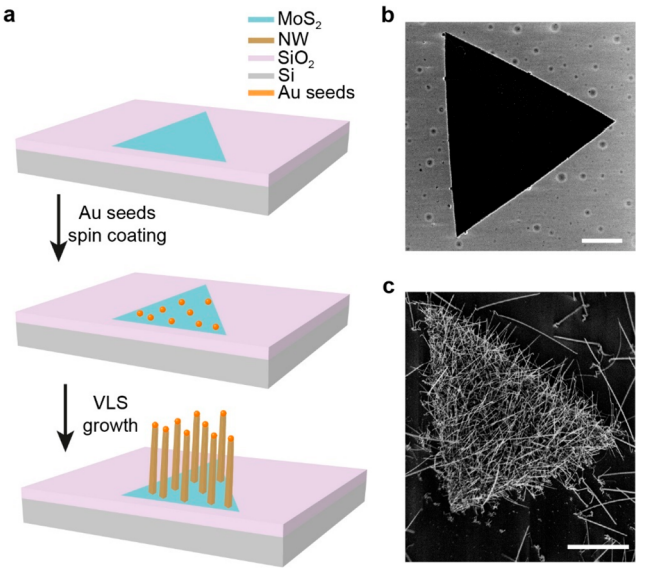

Figure 1. Growth of InP NWs on single-crystal MoS_2. (a) Schematic of process steps for epitaxial growth of NWs on MoS_2. SEM image of (b) a CVD-grown MoS_2 flake and (c) VLS-grown InP NWs on MoS_2 (image taken at 45° tilt). Scale bar: 5 μm.

TEM (HRTEM) image in Figure 2b shows the atomic structure of the NW.

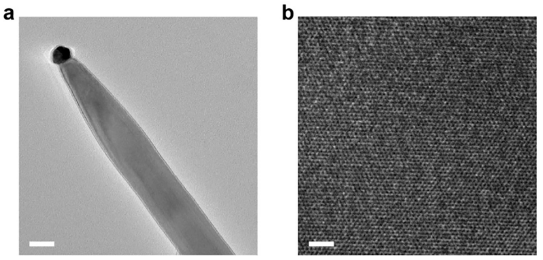

Figure 2. Structural properties of InP NW grown on MoS_2. (a) TEM image and (b) HRTEM image of InP NW with a scale bar of 50 and 1 nm, respectively.

In this experiment, we use the bottom-up VLS growth method for epitaxially growing InP NWs on MoS_2. The VLS NW growth mechanism is usually mediated by the metallic droplets (i.e., Au nanoparticles in this experiment) in the liquid state, which collect the vapor-phase growth species and initiate the nucleation and growth of solid-crystal NWs underneath the droplets. This Au-seeded method allows precise control over the NW diameter, density, and position and reduces the possibility of radial growth.[38] However, the vertical NW growth on MoS_2 largely depends on the V/III ratio, flow rate of the precursors, and growth temperature. With optimized growth parameters, adatoms impinge the surface of MoS_2 under Au seeds and get adsorbed on the site to initiate nucleation and growth of NWs below the seeds. The high-density NW growth usually depends on the sticking coefficient (defined as the ratio of number of adsorbed atoms to the number of migrated or desorbed atoms) and the number of Au seeds on the substrate. MoS_2 has a relatively high sticking coefficient,[23] and Au nanoparticles with PLL treatment ensure an adequate number of seeds on MoS_2. The nanoparticles are mounted on the substrate via MoS_2 fixation, which prevents

https://doi.org/10.1021/acs.chemmater.2c01602
Chem. Mater. 2022, 34, 9055−9061

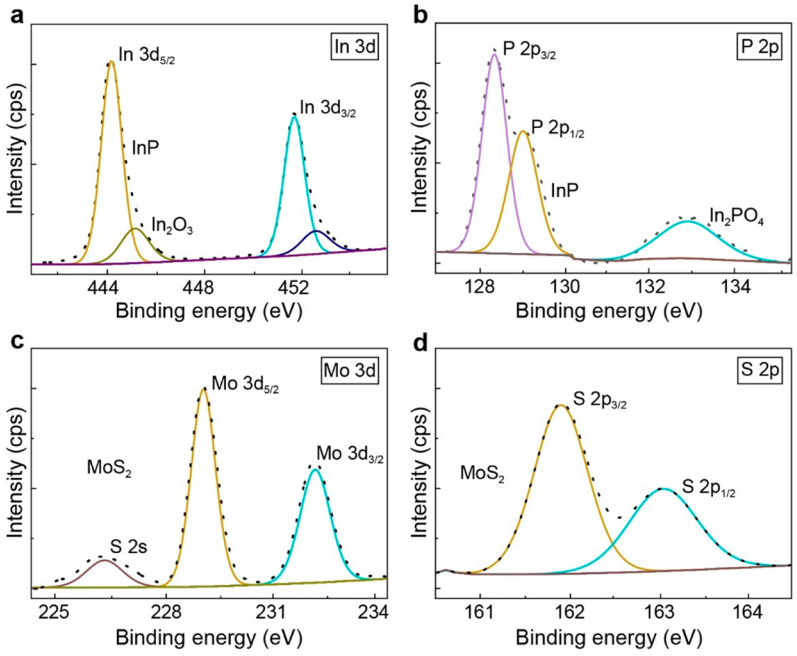

Figure 3. X-ray photoelectron spectra from a NW/MoS_2 heterostructure. (a, b) In-3d and P-2p core level regions. (c, d) Mo-3d and S-2p regions.

Ostwald ripening of these particles. Therefore, the NWs can grow by self-supporting each other, leading to the growth of highly dense and vertical NWs on MoS_2.

The dangling-bond-free surface of any 2D materials makes it difficult to grow III−V NWs with good coverage and adhesion. Only the edges of the 2D materials have dangling bonds which initiate the vdW epitaxial growth of in-plane and out-of-plane NWs around the edges. High-temperature annealing of the 2D materials can create dangling bonds all over the flake to promote the growth of NWs. However, it creates defects in the crystal due to chalcogen vacancies, e.g., sulfur vacancies in MoS_2, which also lead to oxidation.[39] This results in degraded intrinsic properties of the materials and also becomes one of the reasons for forming parasitic islands on MoS_2 (see Figure S2). This also implies that the growth of NWs requiring a relatively higher temperature (close to the growth temperature of the MoS_2) could cause phase alteration and deformation of MoS_2 crystals. Therefore, the thermal stability of MoS_2 during temperature treatment and NW growth is crucial to ensuring high quality of NW/MoS_2 heterostructure-based devices. In our experiment, we use 430 °C for growing InP NWs on MoS_2 flakes. This temperature is suitable for maintaining the crystal stability of MoS_2 during the NW growth and ensures the growth of high-quality InP NWs.

The chemical stability of MoS_2 during the growth of NWs is another crucial factor, which needs to be addressed to ensure the intact quality of MoS_2 after growth. First, we perform PLL treatment and then deposit Au nanoparticles on the MoS_2 flakes. Subsequently, we anneal the MoS_2 flakes at 430 °C for 300 s in the MOCVD chamber while inserting only the TBP precursor into the chamber. We do not observe any change in the Raman and PL spectra of MoS_2, which partially confirms the chemical stability of MoS_2 during NW growth.

Although the thermal and chemical stability of MoS_2 is relatively lower than that of many other 2D materials such as graphene and hBN,[40] MoS_2 possesses a higher potential for 1D integrated high-performance photonic and optoelectronic devices because of its bandgap within the common semiconductor range. Additionally, the surface lattice structure of MoS_2 is also an excellent platform for vdW epitaxial growth of NWs, as MoS_2 has a lattice parameter of 3.16 Å which is approximately 28% larger than that of graphene, making it more favorable for the growth of III−V NWs with large lattice parameters, such as InP. The wurtzite (WZ) and zinc-blende (ZB) phase InP lattice parameters are found to be 4.15 and 5.86 Å, respectively.[41] Therefore, the lattice mismatch between WZ InP-MoS_2 is smaller than that of ZB InP-MoS_2. This suggests that the growth of InP NWs with the WZ phase is more favorable than with ZB.

The high-resolution XPS spectra are acquired from the NW/MoS_2 samples to characterize the composition and quality of the materials. In Figure 3, XPS spectra show emission peaks from In-3d, P-2p, Mo-3d, and P-2p. The core-level spectrum of In-3d in Figure 3a can be deconvoluted into four peaks. Peaks at 444.3 eV (In-$3d_{5/2}$) and 451.8 eV (In-$3d_{3/2}$) are ascribed to InP, whereas peaks at 445.2 and 452.7 eV represent In_2O_3. Figure 3b shows the P-2p spectrum with InP peaks at 128.4 (P-$2p_{3/2}$) and 129.1 eV (P-$2p_{1/2}$), and the $InPO_4$ peak at 133 eV. In both In-3d and P-2p spectra, the relative intensity of InP emission peaks is much higher than that of In_2O_3 and $InPO_4$, which implies that the optimized growth parameters are suitable for suppressing oxide formation and growing good quality NWs on MoS_2. All the heterostructures also contain the characteristic emission peaks of MoS_2. Figure 3c exhibits three major peaks of S-2s, Mo-$3d_{5/2}$, and Mo-$3d_{3/2}$ at 226.3, 229.1, and 232.3 eV, respectively, assigned to MoS_2. As shown in Figure 3d, we observe a doublet from the S-2p peak at 161.9 and 163.1 eV corresponding to S-$2p_{3/2}$ and S-$2p_{1/2}$ attributed to the MoS_2 crystal. All the XPS results agree with previous reports.[42,43]

We further characterize the NW/MoS_2 heterostructure with Raman and PL spectroscopy to investigate their optical response. A comparison of those responses from WZ NWs grown on Si (111) and NW/MoS_2 is also presented in Figure 4. Figure 4a shows the room temperature Raman spectra from NWs and the heterojunction of NW/MoS_2. The longitudinal

https://doi.org/10.1021/acs.chemmater.2c01602
Chem. Mater. 2022, 34, 9055−9061

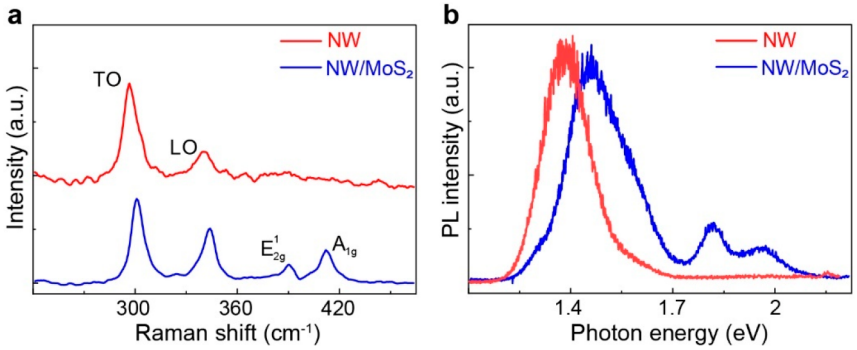

Figure 4. Optical characterizations of the mixed-dimensional heterostructure. (a) Comparison of Raman spectra of InP NWs grown on Si and MoS_2. (b) The PL spectra of NW and NW/MoS_2.

optical (LO) and the transverse optical (TO) phonon modes of InP NWs grown on Si substrate are observed at ∼301 and ∼340 cm^{-1}, respectively. When NWs are grown on MoS_2, we observe similar LO and TO modes with a shift of ∼2.2 and ∼3 cm^{-1}, respectively. In addition, the in-plane E^1_{2g} (∼383.7 cm^{-1}) and out-of-plane A_{1g} (∼403.1 cm^{-1}) Raman modes appear in the Raman spectra that correspond to vibrational modes of MoS_2. The Raman signals from both materials are in good agreement with the previously reported results.[42,44,45] The PL spectra from the samples are shown in Figure 4b. The PL emission peak from the WZ phase of InP NWs grown on Si is observed at ∼1.4 eV (880 nm). However, the peak is blue-shifted by ∼80 meV in the NW/MoS_2 heterostructure. NWs grown on MoS_2 have a smaller effective diameter than those grown on Si due to surface depletion, which could explain the NW PL blue-shift in NW/MoS_2 compared to the NW/Si samples.[46] The average diameter of NWs on MoS_2 is 63.3 ± 5 nm for NW/MoS_2. Few of the measured tapered-shaped NWs have a diameter of ∼30 nm at the middle and ∼20 nm at the top end. Therefore, the quantum confinement effect at the top of the NWs is also possible because the exciton Bohr radius of bulk InP is ∼20 nm. This effect could cause the blue shift of NW PL in NW/MoS_2 sample as reported previously.[47] The heterostructure PL also contains the A-exciton and B-exciton of monolayer MoS_2 at ∼1.82 eV (678 nm) and ∼1.96 eV (631 nm), respectively. The Raman and PL responses of MoS_2 from the NW/MoS_2 heterostructures elucidate the intact quality of the MoS_2 flakes after epitaxial growth of NW on them. Further, as shown in Figure S3, we observe a strong enhancement of absorption from NW/MoS_2 compared to MoS_2 over a broad-spectrum range (∼550 to 800 nm) from the differential reflectivity measurements.

We measure the nonlinear optical responses (i.e., SHG, THG, and HHG) from our NW/MoS_2 heterostructure. In SHG, the incident photons of frequency ω generate new photons of frequency 2ω (inset of Figure 5a). Figure 5a shows the power dependency of SHG intensity from the heterostructure with the excitation wavelength at 800 nm. The calculated slope (∼1.85) confirms the optical process is of second order.[48] The SHG intensities also vary, with excitation wavelengths ranging from 800 to 1500 nm, and are presented in Figure 5b. The signal intensity is highest for 900 nm excitation because the laser energy is in resonance with the InP exciton energy. From the SHG mapping on the heterostructure presented in Figure 5c, we observe that strong SHG signals are generated from all over the sample. As shown in Figure S4, bare MoS_2 shows a 6-fold SHG pattern, whereas the SHG from the heterostructure is independent of the polarization of the pump due to the random growth directions of the NW on MoS_2. However, the intensity of the signals from the heterostructure is twice as strong as compared to bare MoS_2.

In the THG mechanism, the new photons of 3ω are generated from incident photons of ω (inset of Figure 5d). Figure 5d shows the variation in THG intensities from the heterostructure with the incident laser power. The exponent of power-dependent THG signals is about 2.81 with 1300 nm excitation, confirming its third-order optical nonlinearity.[48] Strong THG signals are detected from the heterostructure, with different wavelengths ranging from 1200 to 1500 nm, as shown in Figure 5e. The signals show almost similar strength for all the excitation wavelengths. Interestingly, upon exposure of the heterostructure to a 4000 nm pump laser, we observe fifth- and seventh-order harmonic generations at 800 nm and ∼571 nm, respectively, as shown in Figure 5f. However, the intensity of fifth HG is much stronger than that of seventh HG.

Both InP NWs with noncentrosymmetric crystal structures and MoS_2 contribute to the high-intensity lower-order (SHG and THG) signals and relatively low-intensity HHG signals from the heterostructures. However, NWs contribute more than MoS_2 because they are grown at a high density on MoS_2 which results in more light−matter interactions in NWs than in MoS_2. Therefore, the 6-fold symmetry of SHG from monolayer MoS_2 vanishes at the heterostructure, as shown in Figure S4. However, NW growth density is not uniform on MoS_2, making it difficult to accurately measure the quantitative contribution from each material in the nonlinear optical responses.

Notably, we do not observe any high even-order harmonic generation from the samples. This could indicate that the photophysical process for HHG is different from the lower-order harmonic generation, such as SHG, which is produced due to the nonzero second-order susceptibility resulting from the inversion symmetry breaking points at the surface of the WZ InP NW crystals.[49] However, the absence of higher-order harmonics could theoretically mean that the inversion symmetry is retained, or a different mechanism is responsible for such a semiconductor crystal.[50] Additionally, the even-order HHG from MoS_2 has already been reported.[51] Unexpectedly, we do not observe any influence of MoS_2 even-order HHG in NW/MoS_2 heterostructure. We speculate two possibilities for such results: (1) the reported intensities of the even-order HHG signals from MoS_2 are very small compared to the odd-order HHG signals. The low signal-to-noise ratio in our home-built experimental setup might suppress the intensities of the even-order HHG signals.

https://doi.org/10.1021/acs.chemmater.2c01602
Chem. Mater. 2022, 34, 9055−9061

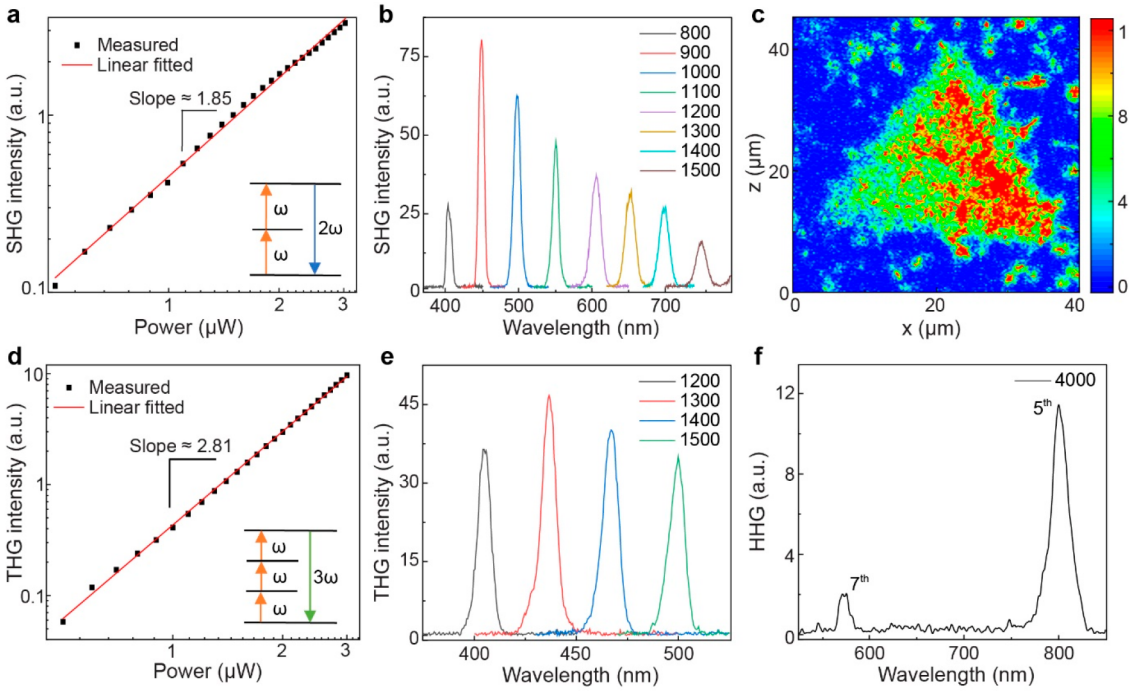

Figure 5. Nonlinear optical responses from the NW/MoS_2 mixed-dimensional heterostructures. (a) Power-dependent SHG intensities for excitation with an 800 nm fundamental beam. Inset shows a schematic of the SHG process. (b) SHG spectra under different excitations. (c) SHG mapping of a sample with 800 nm pulsed laser excitation. (d) THG intensities as a function of the 1300 nm pulse excitation power with a schematic of the THG process in the inset. (e) THG spectra from the sample at a range of discrete wavelengths. (f) Fifth and seventh harmonic generation spectra from the heterostructure with excitation of 4000 nm wavelength.

Therefore, it is difficult to distinguish even-order HHG from the noise level of the system. Additionally, the input power was very close to the burning threshold of the samples. Therefore, a further increase in the laser power was damaging to our samples. (2) The light−matter interactions in NW and MoS_2 might suppress the even-order HHG from the heterostructures because of their distinctive crystal symmetries and orientations. Therefore, it requires further theoretical and experimental investigations to explain the unusual phenomenon.

Our findings show a simple way to fabricate InP-NW/MoS_2 mixed-dimensional heterostructures. The nonlinear responses, especially the HHG from the NW/MoS_2 heterostructure, could create new possibilities for numerous applications (e.g., lasers, electro-optic modulators, and frequency converters) of mixed-dimensional heterostructures.

CONCLUSION

In this work, we demonstrate the successful growth of InP NWs on MoS_2. The high yield of vertical NWs is achieved through optimized growth parameters. The low-temperature NW growth process ensures the stability of MoS_2 and produces high-quality NWs. Further, we show the excellent Raman and PL responses from the heterostructure. Our mixed-dimensional heterostructures exhibit strong nonlinear optical responses (SHG, THG, and HHG), promising numerous technological advances in photonics.

MATERIALS AND METHODS

For structural analysis, transmission electron microscopy (TEM) measurement of NWs is carried out with a JEOL 2200FS double aberration-corrected field emission gun microscope operated at 200 kV. As-grown NWs are transferred on a 400-mesh copper grid having 3 mm diameter and covered with a carbon film on one side to support the NWs.

To investigate the chemical composition and chemical bonding states of the samples, X-ray photoelectron spectroscopy (XPS) is performed in the Kratos Axis Ultra system with a monochromatic Al Kα (1486.96 eV) source. The wide scans are performed with a 300 × 700 μm analysis area. The high-resolution scans are performed with a 20 eV pass energy and a 0.1 eV energy step. All spectra are calibrated by the C 1s peak at 284.6 eV.

The room-temperature Raman and PL spectra are recorded in a backscattering geometry with a confocal micro-Raman system (WITec alpha300 RA+). In both measurements, a 100× objective with a numerical aperture of 0.7 is used for illuminating with a 532 nm laser at a 2 mW power. The morphologies of MoS_2 and NW/MoS_2 are examined by a scanning electron microscope (SEM) (Zeiss Supra 40).

For SHG, THG, and HHG, an ultrafast femtosecond laser (Spectra-Physics, TOPAS) is used. The pulse width and the repetition rate of the laser are ∼230 fs and 2 kHz, respectively. The laser is focused on the sample through an objective lens (40×, 0.75 NA) with a spot size of ∼2.5 μm. The nonlinear responses from the samples are detected in reflection configuration by a photomultiplier tube (PMT) following a monochromator (Andor 328i). The SHG mapping is taken using a home-build multiphoton setup. For this measurement, the repetition rate of the ultrafast laser at 800 nm is 84.49 MHz. The beam is focused on the sample with an objective lens (40×, 0.75 NA), and the SHG is collected by the PMT, followed by multiple optical filters to block the seed laser.

ASSOCIATED CONTENT

Supporting Information

The Supporting Information is available free of charge at https://pubs.acs.org/doi/10.1021/acs.chemmater.2c01602.

Schematic of a dual-zone CVD system for growing MoS_2, SEM image of InP NW grown on annealed MoS_2,

https://doi.org/10.1021/acs.chemmater.2c01602
Chem. Mater. 2022, 34, 9055−9061

differential reflectivity comparison of MoS_2 and NW/MoS_2, polarization dependent SHG from MoS_2 and NW/MoS_2 samples, SHG from a MoS_2 sample, and typical NW SEM images from the NW/MoS_2 samples (PDF)

AUTHOR INFORMATION

Corresponding Authors

Abde Mayeen Shafi − *Department of Electronics and Nanoengineering, Aalto University, FI-02150 Espoo, Finland;* orcid.org/0000-0003-2619-3077; Email: abde.shafi@aalto.fi

Harri Lipsanen − *Department of Electronics and Nanoengineering, Aalto University, FI-02150 Espoo, Finland;* orcid.org/0000-0003-2487-4645; Email: harri.lipsanen@aalto.fi

Authors

Susobhan Das − *Department of Electronics and Nanoengineering, Aalto University, FI-02150 Espoo, Finland*

Vladislav Khayrudinov − *Department of Electronics and Nanoengineering, Aalto University, FI-02150 Espoo, Finland;* orcid.org/0000-0002-4125-6104

Er-Xiong Ding − *Department of Electronics and Nanoengineering, Aalto University, FI-02150 Espoo, Finland*

Md Gius Uddin − *Department of Electronics and Nanoengineering, Aalto University, FI-02150 Espoo, Finland*

Faisal Ahmed − *Department of Electronics and Nanoengineering, Aalto University, FI-02150 Espoo, Finland*

Zhipei Sun − *Department of Electronics and Nanoengineering, Aalto University, FI-02150 Espoo, Finland; QTF Centre of Excellence, Department of Applied Physics, Aalto University, FI-00076 Espoo, Finland;* orcid.org/0000-0002-9771-5293

Complete contact information is available at: https://pubs.acs.org/10.1021/acs.chemmater.2c01602

Notes

The authors declare no competing financial interest.

ACKNOWLEDGMENTS

This research was supported by supported by the GrapheneCore3 number 881603 and Academy of Finland [grant no. 320167 (PREIN Flagship - Aalto University)]. V.K. acknowledges the support of Aalto University Doctoral School, Walter Ahlström Foundation, Elektroniikkainsinöörien Säätiö, Sähköinsinööriliiton Säätiö, Nokia Foundation, Finnish Foundation for Technology Promotion (Tekniikan Edistämis- säätiö), Waldemar von Frenckell's Foundation, and Kansallis- Osake-Pankki fund. The authors acknowledge Micronova for fabrication and characterization infrastructure and provision of facilities of Aalto University at OtaNano − Nanomicroscopy Center (Aalto-NMC).

REFERENCES

(1) Novoselov, K. S.; Geim, A. K.; Morozov, S. V.; Jiang, D. E.; Zhang, Y.; Dubonos, S. V.; Grigorieva, I. V.; Firsov, A. A. Electric Field Effect in Atomically Thin Carbon Films. *Science* **2004**, *306* (5696), 666−669.

(2) Das, S.; Sebastian, A.; Pop, E.; McClellan, C. J.; Franklin, A. D.; Grasser, T.; Knobloch, T.; Illarionov, Y.; Penumatcha, A. V.; Appenzeller, J.; Chen, Z.; Zhu, W.; Asselberghs, I.; Li, L.-J.; Avci, U. E.; Bhat, N.; Anthopoulos, T. D.; Singh, R. Transistors Based on Two-Dimensional Materials for Future Integrated Circuits. *Nat. Electron.* **2021**, *4* (11), 786−799.

(3) Schmidt, H.; Wang, S.; Chu, L.; Toh, M.; Kumar, R.; Zhao, W.; Castro Neto, A. H.; Martin, J.; Adam, S.; Özyilmaz, B.; Eda, G. Transport Properties of Monolayer MoS_2 Grown by Chemical Vapor Deposition. *Nano Lett.* **2014**, *14* (4), 1909−1913.

(4) Liu, X.; Hersam, M. C. 2D Materials for Quantum Information Science. *Nat. Rev. Mater.* **2019**, *4* (10), 669−684.

(5) Wang, Q. H.; Kalantar-Zadeh, K.; Kis, A.; Coleman, J. N.; Strano, M. S. Electronics and Optoelectronics of Two-Dimensional Transition Metal Dichalcogenides. *Nat. Nanotechnol.* **2012**, *7* (11), 699−712.

(6) Choi, W.; Choudhary, N.; Han, G. H.; Park, J.; Akinwande, D.; Lee, Y. H. Recent Development of Two-Dimensional Transition Metal Dichalcogenides and Their Applications. *Mater. Today* **2017**, *20* (3), 116−130.

(7) Ahmed, F.; Shafi, A. M.; Mackenzie, D. M. A.; Qureshi, M. A.; Fernandez, H. A.; Yoon, H. H.; Uddin, M. G.; Kuittinen, M.; Sun, Z.; Lipsanen, H. Multilayer $MoTe_2$ Field-Effect Transistor at High Temperatures. *Adv. Mater. Interfaces* **2021**, *8* (22), 2100950.

(8) Zhang, L.; Zunger, A. Evolution of Electronic Structure as a Function of Layer Thickness in Group-VIB Transition Metal Dichalcogenides: Emergence of Localization Prototypes. *Nano Lett.* **2015**, *15* (2), 949−957.

(9) Geim, A. K.; Grigorieva, I. V. Van Der Waals Heterostructures. *Nature* **2013**, *499* (7459), 419−425.

(10) Das, S.; Robinson, J. A.; Dubey, M.; Terrones, H.; Terrones, M. Beyond Graphene: Progress in Novel Two-Dimensional Materials and van Der Waals Solids. *Annu. Rev. Mater. Res.* **2015**, *45* (1), 1−27.

(11) Jariwala, D.; Marks, T. J.; Hersam, M. C. Mixed-Dimensional van Der Waals Heterostructures. *Nat. Mater.* **2017**, *16* (2), 170−181.

(12) Liu, Y.; Huang, Y.; Duan, X. Van Der Waals Integration before and beyond Two-Dimensional Materials. *Nature* **2019**, *567* (7748), 323−333.

(13) Johansson, J.; Karlsson, L. S.; Patrik, T.; Svensson, C.; Mårtensson, T.; Wacaser, B. A.; Deppert, K.; Samuelson, L.; Seifert, W. Structural Properties of ⟨111⟩ B - Oriented III−V Nanowires. *Nat. Mater.* **2006**, *5* (7), 574−580.

(14) Lim, S. K.; Brewster, M.; Qian, F.; Li, Y.; Lieber, C. M.; Gradečak, S. Direct Correlation between Structural and Optical Properties of III−v Nitride Nanowire Heterostructures with Nanoscale Resolution. *Nano Lett.* **2009**, *9* (11), 3940−3944.

(15) Hrachowina, L.; Anttu, N.; Borgström, M. T. Wafer-Scale Synthesis and Optical Characterization of InP Nanowire Arrays for Solar Cells. *Nano Lett.* **2021**, *21* (17), 7347−7353.

(16) Anttu, N.; Mäntynen, H.; Sadi, T.; Matikainen, A.; Turunen, J.; Lipsanen, H. Comparison of Absorption Simulation in Semiconductor Nanowire and Nanocone Arrays with the Fourier Modal Method, the Finite Element Method, and the Finite-Difference Time-Domain Method. *Nano Express* **2020**, *1* (3), 030034.

(17) Shin, J. C.; Mohseni, P. K.; Yu, K. J.; Tomasulo, S.; Montgomery, K. H.; Lee, M. L.; Rogers, J. A.; Li, X. Heterogeneous Integration of InGaAs Nanowires on the Rear Surface of Si Solar Cells for Efficiency Enhancement. *ACS Nano* **2012**, *6* (12), 11074−11079.

(18) Dhaka, V.; Haggren, T.; Jussila, H.; Jiang, H.; Kauppinen, E.; Huhtio, T.; Sopanen, M.; Lipsanen, H. High Quality GaAs Nanowires Grown on Glass Substrates. *Nano Lett.* **2012**, *12* (4), 1912−1918.

(19) Khayrudinov, V.; Remennyi, M.; Raj, V.; Alekseev, P.; Matveev, B.; Lipsanen, H.; Haggren, T. Direct Growth of Light-Emitting III−V Nanowires on Flexible Plastic Substrates. *ACS Nano* **2020**, *14* (6), 7484−7491.

(20) Mohseni, P. K.; Behnam, A.; Wood, J. D.; English, C. D.; Lyding, J. W.; Pop, E.; Li, X. $In_xGa_{1-x}As$ Nanowire Growth on Graphene: Van Der Waals Epitaxy Induced Phase Segregation. *Nano Lett.* **2013**, *13* (3), 1153−1161.

(21) Berdnikov, Y.; Sibirev, N. V.; Khayrudinov, V.; Alaferdov, A.; Moshkalev, S.; Ubyivovk, E. V.; Lipsanen, H.; Bouravleuv, A. Growth of GaAs Nanowire−Graphite Nanoplatelet Hybrid Structures. *CrystEngComm* **2019**, *21* (41), 6165−6172.

(22) Hong, Y. J.; Lee, W. H.; Wu, Y.; Ruoff, R. S.; Fukui, T. Van Der Waals Epitaxy of InAs Nanowires Vertically Aligned on Single-Layer Graphene. *Nano Lett.* **2012**, *12* (3), 1431−1436.
(23) Baboli, M. A.; Abrand, A.; Burke, R. A.; Fedorenko, A.; Wilhelm, T. S.; Polly, S. J.; Dubey, M.; Hubbard, S. M.; Mohseni, P. K. Mixed-Dimensional InAs Nanowire on Layered Molybdenum Disulfide Heterostructures via Selective-Area van Der Waals Epitaxy. *Nanoscale Adv.* **2021**, *3* (10), 2802−2811.
(24) Uddin, M. G.; Das, S.; Shafi, A. M.; Khayrudinov, V.; Ahmed, F.; Fernandez, H.; Du, L.; Lipsanen, H.; Sun, Z. Engineering the Dipole Orientation and Symmetry Breaking with Mixed-Dimensional Heterostructures. *Adv. Sci.* **2022**, *9*, 2200082.
(25) Shafi, A. M.; Ahmed, F.; Fernandez, H. A.; Uddin, M. G.; Cui, X.; Das, S.; Dai, Y.; Khayrudinov, V.; Yoon, H. H.; Du, L.; Sun, Z.; Lipsanen, H. Inducing Strong Light−Matter Coupling and Optical Anisotropy in Monolayer MoS_2 with High Refractive Index Nanowire. *ACS Appl. Mater. Interfaces* **2022**, *14* (27), 31140−31147.
(26) Yuan, X. I. Y.; Liu, K.; Skalsky, S.; Parkinson, P.; Fang, L.; He, J.; Tan, H. H.; Jagadish, C. Carrier Dynamics and Recombination Mechanisms in InP Twinning Superlattice Nanowires. *Opt. Express* **2020**, *28* (11), 16795−16804.
(27) Wallentin, J.; Anttu, N.; Asoli, D.; Huffman, M.; Åberg, I.; Magnusson, M. H.; Siefer, G.; Fuss-Kailuweit, P.; Dimroth, F.; Witzigmann, B.; Xu, H. Q.; Samuelson, L.; Deppert, K.; Borgström, M. T. InP Nanowire Array Solar Cells Achieving 13.8% Efficiency by Exceeding the Ray Optics Limit. *Science* **2013**, *339* (6123), 1057−1060.
(28) Duan, X.; Huang, Y.; Cui, Y.; Wang, J.; Lieber, C. M. Indium Phosphide Nanowires as Building Blocks for Nanoscale Electronic and Optoelectronic Devices. *Nature* **2001**, *409* (6816), 66−69.
(29) Wang, J.; Gudiksen, M. S.; Duan, X.; Cui, Y.; Lieber, C. M. Highly Polarized Photoluminescence and Photodetection from Single Indium Phosphide Nanowires. *Science* **2001**, *293* (5534), 1455−1457.
(30) Gao, Q.; Saxena, D.; Wang, F.; Fu, L.; Mokkapati, S.; Guo, Y.; Li, L.; Wong-Leung, J.; Caroff, P.; Tan, H. H.; Jagadish, C. Selective-Area Epitaxy of Pure Wurtzite InP Nanowires: High Quantum Efficiency and Room-Temperature Lasing. *Nano Lett.* **2014**, *14* (9), 5206−5211.
(31) Mak, K. F.; Lee, C.; Hone, J.; Shan, J.; Heinz, T. F. Atomically Thin MoS_2: A New Direct-Gap Semiconductor. *Phys. Rev. Lett.* **2010**, *105* (13), 136805.
(32) Salehzadeh, O.; Djavid, M.; Tran, N. H.; Shih, I.; Mi, Z. Optically Pumped Two-Dimensional MoS_2 Lasers Operating at Room-Temperature. *Nano Lett.* **2015**, *15* (8), 5302−5306.
(33) Liu, J.; Nie, H.; Yan, B.; Yang, K.; Yang, H.; Khayrudinov, V.; Lipsanen, H.; Zhang, B.; He, J. Nonlinear Optical Absorption Properties of InP Nanowires and Applications as a Saturable Absorber. *Photonics Res.* **2020**, *8* (6), 1035.
(34) Malard, L. M.; Alencar, T. V.; Barboza, A. P. M.; Mak, K. F.; de Paula, A. M. Observation of Intense Second Harmonic Generation from MoS_2 Atomic Crystals. *Phys. Rev. B Condens. Matter Mater.* **2013**, *87* (20), 201401.
(35) Autere, A.; Jussila, H.; Dai, Y.; Wang, Y.; Lipsanen, H.; Sun, Z. Nonlinear Optics with 2D Layered Materials. *Adv. Mater.* **2018**, *30* (24), 1705963.
(36) Bai, X.; Li, S.; Das, S.; du; Dai, Y.; Yao, L.; Raju, R.; Du, M.; Lipsanen, H.; Sun, Z. Single-Step Chemical Vapour Deposition of Anti-Pyramid MoS_2/WS_2 Vertical Heterostructures. *Nanoscale* **2021**, *13*, 4537−4542.
(37) Yang, H.; Khayrudinov, V.; Dhaka, V.; Jiang, H.; Autere, A.; Lipsanen, H.; Sun, Z.; Jussila, H. Nanowire Network−based Multifunctional All-optical Logic Gates. *Sci. Adv.* **2018**, *4* (7), eaar7954.
(38) Wallentin, J.; Kriegner, D.; Stangl, J.; Borgström, M. T. Au-Seeded Growth of Vertical and In-Plane III−V Nanowires on Graphite Substrates. *Nano Lett.* **2014**, *14* (4), 1707−1713.
(39) Bandaru, N.; Kumar, R. S.; Sneed, D.; Tschauner, O.; Baker, J.; Antonio, D.; Luo, S.-N.; Hartmann, T.; Zhao, Y.; Venkat, R. Effect of Pressure and Temperature on Structural Stability of MoS_2. *J. Phys. Chem. C* **2014**, *118* (6), 3230−3235.
(40) Hong, Y. J.; Saroj, R. K.; Park, W. I.; Yi, G.-C. One-Dimensional Semiconductor Nanostructures Grown on Two-Dimensional Nanomaterials for Flexible Device Applications. *APL Mater.* **2021**, *9* (6), 060907.
(41) Faria Junior, P. E.; Sipahi, G. M. Band Structure Calculations of InP Wurtzite/Zinc-Blende Quantum Wells. *J. Appl. Phys.* **2012**, *112* (10), 103716.
(42) Tian, Z.; Yuan, X.; Zhang, Z.; Jia, W.; Zhou, J.; Huang, H.; Meng, J.; He, J.; Du, Y. Thermodynamics Controlled Sharp Transformation from InP to GaP Nanowires via Introducing Trace Amount of Gallium. *Nanoscale Res. Lett.* **2021**, *16* (1), 1−9.
(43) Senthilkumar, V.; Tam, L. C.; Kim, Y. S.; Sim, Y.; Seong, M.-J.; Jang, J. I. Direct Vapor Phase Growth Process and Robust Photoluminescence Properties of Large Area MoS_2 Layers. *Nano Res.* **2014**, *7* (12), 1759−1768.
(44) Lee, C.; Yan, H.; Brus, L. E.; Heinz, T. F.; Hone, J.; Ryu, S. Anomalous Lattice Vibrations of Single- and Few-Layer MoS_2. *ACS Nano* **2010**, *4* (5), 2695−2700.
(45) Li, H.; Zhang, Q.; Yap, C. C. R.; Tay, B. K.; Edwin, T. H. T.; Olivier, A.; Baillargeat, D. From Bulk to Monolayer MoS_2: Evolution of Raman Scattering. *Adv. Funct. Mater.* **2012**, *22* (7), 1385−1390.
(46) Mattila, M.; Hakkarainen, T.; Lipsanen, H.; Jiang, H.; Kauppinen, E. I. Enhanced Luminescence from Catalyst-Free Grown InP Nanowires. *Appl. Phys. Lett.* **2007**, *90* (3), 033101.
(47) Ren, P.; Xu, J.; Wang, Y.; Zhuang, X.; Zhang, Q.; Zhou, H.; Wan, Q.; Shan, Z.; Zhu, X.; Pan, A. Synthesis and Optical Properties of InP Quantum Dot/Nanowire Heterostructures. *Phys. Status Solidi A* **2013**, *210* (9), 1898−1902.
(48) Boyd, R. W. *Nonlinear Optics*; 3rd ed.; Academic Press: New York, 2008.
(49) Wang, F.; Reece, P. J.; Paiman, S.; Gao, Q.; Tan, H. H.; Jagadish, C. Nonlinear Optical Processes in Optically Trapped InP Nanowires. *Nano Lett.* **2011**, *11* (10), 4149−4153.
(50) Hagen, M. K.; Koch, S. W. Probing Intervalence Band Coupling via High-Harmonic Generation in Binary Zinc-Blende Semiconductors. *Phys. Status Solidi Rapid Res. Lett.* **2021**, *15* (11), 2100397.
(51) Liu, H.; Li, Y.; You, Y. S.; Ghimire, S.; Heinz, T. F.; Reis, D. A. High-Harmonic Generation from an Atomically Thin Semiconductor. *Nat. Phys.* **2017**, *13* (3), 262−265.

https://doi.org/10.1021/acs.chemmater.2c01602
Chem. Mater. 2022, 34, 9055−9061